Journal of the Mechanics and Physics of Solids 131 (2019) 1–19

Contents lists available at ScienceDirect

Journal of the Mechanics and Physics of Solids

journal homepage: www.elsevier.com/locate/jmps

Rate-dependent traction-separation relations for a silicon/epoxy interface informed by experiments and bond rupture kinetics

Tianhao Yang[a], Xingwei Yang[b], Rui Huang[a], Kenneth M. Liechti[a,*]

[a] Department of Aerospace Engineering and Engineering Mechanics, University of Texas, Austin, TX 78712, USA
[b] Department of Modern Mechanics, University of Science and Technology of China, Hefei, Anhui, PR China

ARTICLE INFO

Article history:
Received 16 January 2019
Revised 3 June 2019
Accepted 23 June 2019
Available online 25 June 2019

Keywords:
Interfacial fracture
Rate dependence
Cohesive zone model
Bond rupture kinetics
Traction-separation relations

ABSTRACT

In this work, double cantilever beam specimens were used to investigate the rate-dependent fracture of a silicon/epoxy interface. Fracture experiments were conducted at 5 different separation rates, ranging from 0.042 to 8.5 mm/s. For each separation rate, the interfacial properties were extracted by a beam on elastic foundation model and an iterative method, assuming a bilinear traction-separation relation. Rate dependence is observed for the silicon/epoxy interface as both the interfacial toughness and strength increased with the separation rates, which is opposite to the rate dependent fracture behavior of the bulk epoxy in its glassy state. Motivated by this observation, a rate-dependent cohesive zone model is proposed based on a thermally activated bond rupture mechanism. This model relates the interfacial fracture to the breakage of molecular bonds at the interface, and the rate effect develops naturally from the kinetics of damage evolution via the statistical concept of bond survival probability. The double cantilever beam problem with the interfacial bond rupture kinetics was then solved numerically, and the model parameters were extracted by fitting the numerical results to the experimental data. Ideally, this model should be able to explain and predict the rate-dependent fracture of a specific interface (e.g., silicon/epoxy interface) with four parameters, including the bond energy, the critical stress, the initial stiffness and a time scale. However, in order to fit the experimental data, the critical stress had to be adjusted in the present study. Nevertheless, this mechanism-based cohesive zone model offers a promising approach for modeling the rate-dependent fracture, which may also incorporate other mechanisms in future studies.

1. Introduction

The rate dependence of the delamination of interfaces has been exploited for selective delamination in transfer printing (Feng et al., 2007) and dry transfer of graphene from its growth substrate to an epoxy (Na et al., 2015; Yoon et al., 2012). In both cases, an increase in the separation rate increased the interfacial toughness, but for different reasons. Transfer printing made use of a polymer in its rubbery state and increasing the separation rate could be (Knauss, 1975) and has been (Cheng et al., 2012) linked to bulk viscoelastic processes. In contrast, the cited examples of dry transfer made use of a glassy polymer (epoxy) whose bulk fracture toughness decreases with increasing separation rate (Makhecha et al., 2009).

* Corresponding author.
E-mail address: kml@mail.utexas.edu (K.M. Liechti).

https://doi.org/10.1016/j.jmps.2019.06.013
0022-5096/

The increasing toughness associated with delamination between interfaces involving glassy polymers must therefore be attributed to the interfacial behavior of such polymers (Rakestraw et al., 1995). A number of potential mechanisms for this behavior have been proposed. One idea is that glassy polymers develop an interphase region in the vicinity of their interface with another material whose properties differ from those of the bulk (Drzal, 1986, 1990; Sharpe, 1972). Ligament formation and polymer chain pullout have also been considered (Swadener et al., 1999). This paper focuses on the rate dependent fracture of a silicon/epoxy interface and proposes a rate-dependent cohesive zone model based on a thermally activated interfacial bond rupture mechanism.

Interfacial fracture in layered structures has been addressed and discussed in detail with respect to elastic fracture phenomena assuming small-scale yielding or process zones (Hutchinson and Suo, 1991). The linear elastic fracture mechanics-based method works well in predicting the propagation of an existing delamination. However, limitations to this approach can arise for fracture with large yielding or process zones where nonlinear effects are critically important. Cohesive zone modeling has been commonly utilized to approximate the nonlinear fracture phenomena and to predict initiation and propagation of interfacial cracks. The concept of the cohesive zone model was first presented by Dugdale (1960) and Barenblatt (1962) to investigate yielding at a crack tip and account for finite strength of brittle materials. One of the fundamental aspects in cohesive zone modeling is to define a traction-separation relation across the interface, which approximates the nonlinear fracture process. The methods to extract traction-separation relations are generally classified as either a direct method (Gowrishankar et al., 2012; Sørensen and Jacobsen, 2003; Sorensen et al., 2008; Wu et al., 2016; Zhu et al., 2009) or an iterative method (Cox and Marshall, 1991; Gowrishankar et al., 2012; Li et al., 2005; Mello and Liechti, 2006; Sorensen et al., 2008). The direct method usually requires measurements at or near the crack tip, such as crack tip opening displacements and crack extension, and thus is limited by resolution issues. The iterative method, on the other hand, depends on far field measurements, such as force and displacement at the loading point, and determines traction-separation relations by comparing numerical results with experimental data.

Rate-dependent fracture of polymers and their interfaces may result from viscoelasticity and damage processes. The damage processes are often confined in a small region around the crack tip and may be described by rate-dependent traction-separation relations, which are the focus of this paper. Previously, Knauss and Losi (1993) proposed a rate-dependent crack propagation model for craze-like fracture in polymers and failure of a bonded joint with a thin adhesive layer, where a nonlinear viscoelastic constitutive model was used in a narrow cohesive zone and the effect of void formation was accounted for by an experimentally determined damage function. Later, Rahul-Kumar et al. (1999) implemented a family of cohesive elements with rate-independent and rate-dependent traction-separation relations for fracture at polymer interfaces. They described two rate-dependent cohesive zone models, one based on a rate-dependent craze-like fracture model (Knauss and Losi, 1993) and the other based on a generalized viscous fluid model (de Gennes, 1996; Kogan et al., 1996; Xu et al., 1991). The rate-dependent toughness of elastic-viscoplastic materials was analyzed in Landis et al. (2000) using a viscoplastic traction-separation relation that follows a similar functional form as the constitutive relation for the bulk material. Based on their experiments, Liechti and Wu (2001) used a nonlinear viscoelastic Kelvin unit to simulate rate-dependent cohesive forces between rubber and steel under mixed-mode loading at different rates. Similarly, a nonlinear spring in parallel with a linear Maxwell element was used in a rate-dependent cohesive zone model (Xu et al., 2003) for crack growth in adhesive joints. Zhang et al. (2003) proposed a cohesive zone model consisting of a plastic region and a damage region, each of which was described by a rate-dependent traction-separation relation with a linear viscosity. Giambanco and Fileccia Scimemi (2006) formulated a rate-dependent interface model in the framework of viscoplasticity considering hardening, softening and friction in presence of shear and tensile tractions. Based on compact tension tests of bulk epoxy, Makhecha et al. (2009) developed two rate-dependent traction-separation relations, each with one rate-dependent parameter, to simulate the stick-slip fracture in an adhesively bonded aluminum double cantilever beam. A direct approach was used to determine the mode I and mode II traction-separation relations of a polyurea/steel interface (Zhu et al., 2009), which exhibited strong rate dependence. Marzi et al. (2009) used bilinear traction-separation relations with rate-dependent parameters directly extracted from experiments for failure of structural adhesive joints loaded in mode I. A similar approach was followed by Mohammed et al. (2016) in their study of pressure-sensitive adhesives, which also suggested that the rate dependence in their experiments was dominated by the rate-dependent interfacial properties, rather than the bulk viscoelasticity.

The traction-separation relations are essentially continuum descriptions of the bimaterial interfaces subject to tensile and/or shear tractions. Such descriptions are phenomenological but could, in principle, be linked to atomistic or molecular mechanisms (Ghatak et al., 2000; Kogan et al., 1996; Rahul-Kumar et al., 1999; Spearot et al., 2004; Xu et al., 1991), which would provide more fundamental descriptions of the interactions during fracture. For example, van der Waals interactions between a graphene monolayer and silicon oxide can be calculated by first-principle density functional theory with dispersion corrections and then effectively represented by an interfacial potential that leads to a traction-separation relation (Gao et al., 2014). At a finite temperature ($T > 0\,K$), MD simulations showed that thermal rippling of graphene leads to a temperature-dependent traction-separation relation (Wang et al., 2016). For polymer interfaces, the pull-out of molecular chains was proposed as the underlying mechanism for the rate-dependent traction-separation relations (Kogan et al., 1996; Xu et al., 1991). More specifically for an epoxy/silica interface, a multiscale approach was used to predict the stiffness, strength, and toughness in a bilinear traction-separation relation based on MD simulations and a worm-like chain model (Lau et al., 2012). On the other hand, a kinetic theory of bond dissociation was adopted by Bell (1978) to study cell adhesion, which has been extended by others to study polymer interfaces (Büyüköztürk et al., 2011; Ghatak et al., 2000)

and other molecular bonds (Evans and Ritchie, 1997; Pobelov et al., 2017; Wiita et al., 2006) including protein unfolding (Ackbarow et al., 2007). More recently, a kinetic bond breaking model was developed by Freund (2014) along with the statistical concept of bond survival probability for the growth of a planar crack in a brittle material, which makes it possible to relate the commonly measured fracture properties to the underlying bond parameters. A similar statistical model was proposed by Qian et al. (2017) to describe rate-dependent peeling of an elastic strip from a flat substrate with an array of non-covalent molecular bonds.

This paper focuses on rate dependent fracture of a silicon/epoxy interface under nominally mode I conditions. The experiments were conducted using symmetric double cantilever beam (DCB) specimens. We take three approaches to analyze the DCB experiments. First, a beam on elastic foundation (BEF) model is used to determine the stiffness of the interface and fracture resistance curves (R-curves). Next, assuming a bilinear traction-separation relation for the interface, an iterative approach is employed to numerically extract the parameters (strength and toughness) from the experimental data. The third approach is based on a kinetic bond rupture model. Unlike the first two approaches, where the extracted model parameters are rate dependent, the third approach considers interfacial fracture as a result of thermally activated bond rupture processes, which are intrinsically rate dependent (and time/history dependent as well). The remainder of this paper is organized as follows. Section 2 presents the experimental method, followed by a series of methods for data analysis and modeling in Section 3. The results are presented in Section 4 with discussions. We conclude in Section 5 with a summary of main findings.

2. Experiment

A sandwich DCB specimen consisting of two layers of silicon bonded by an epoxy, was adopted for the experiments in this study (Fig. 1a). The silicon strips were bonded to aluminum tabs at the opening end (Fig. 1a), which were connected to a servo hydraulic, universal testing machine through two pins. The displacement rate control was applied at the opening end of the specimen and the bonded end was free. The reaction force was measured by a load cell (45 N range, Omega). N-type silicon strips (Young's modulus 169 GPa and Poisson's ratio 0.22) with (111) surfaces were used because this plane has the smoothest surface and most dense atomic arrangement, thereby also minimizing any fracture of the silicon. A dicing machine (Disco, DAD 321) was used to cut 100 mm diameter silicon wafers (500 $\pm$ 25 µm in thickness) into 40 $\times$ 5 mm strips, which were then cleaned individually by ultra-sonication in de-ionized water to remove any particles that might have accumulated during the dicing procedure. One silicon adherend was coated with an Au/Pd film (~15 nm) from one end of the strip to a length of 15–20 mm. The purpose of the Au/Pd coating is to form a sharp crack between silicon and epoxy, with minimal damage ahead of the initial crack front, because the adhesion energy between Au/Pd coating and the epoxy is relatively small (~0.07 J/m^2) compared to the silicon/epoxy interface. The sharp crack reduces the crack blunting effect by minimizing the shear yielding around the crack tip (Kinloch and Williams, 1980; Williams and Hodgkinson, 1981), and thus plane strain behavior dominates and steady-state crack growth is expected. The effect of the coating layer can be observed from the measured load-displacement curve as seen in Fig. 1b. When there is no coating, the force required to initiate a crack from the bimaterial corner at the epoxy terminus is apparently larger than that required for the sharp crack produced by the Au/Pd coating. The two responses eventually converge for steady-state crack growth. Interestingly, this blunt crack initiation effect was only observable for the largest separation rate (8.5 mm/s). Therefore, the Au/Pd coating was not needed for the other lower separation rates.

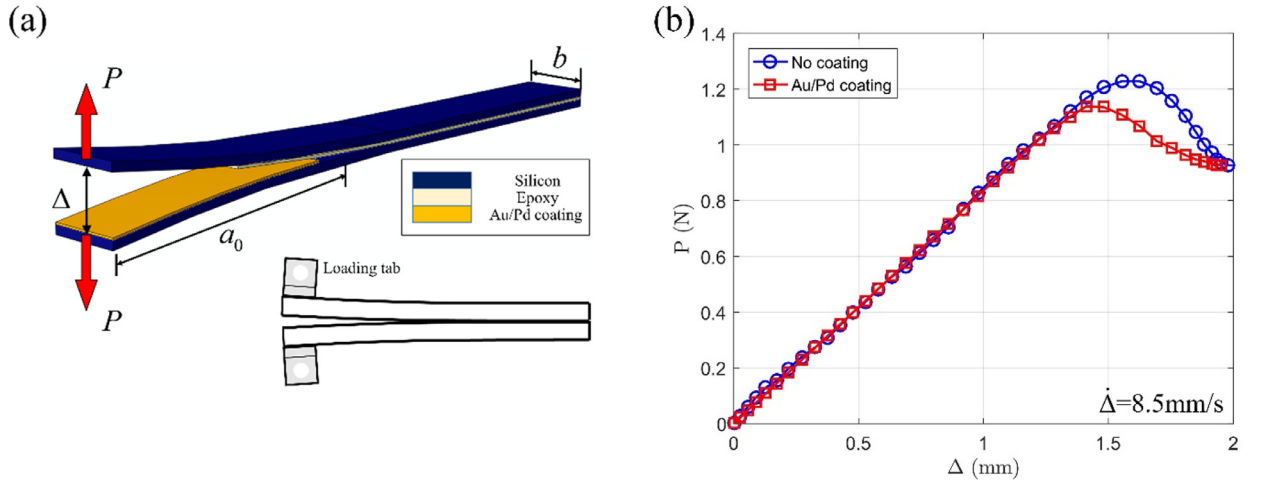

Fig. 1. (a) Schematic of a DCB specimen and loading tabs; (b) Load-displacement curves of two specimens with the same initial crack length, one with the Au/Pd coating for a sharp initial crack and the other without a coating.

The epoxy (EP30, Master Bond Inc.) was prepared by mixing the resin and hardener in a 4:1 ratio by weight. The mixture of resin and hardener was degassed in a vacuum chamber to remove trapped bubbles formed during the mixing process. To prepare the DCB specimen, a bead of the degassed epoxy was dropped on the silicon surface and spread out with a cover glass. Then the other silicon adherend partially coated with Au/Pd (if needed) was compressed with a weight to help further spread epoxy into a 5 to 40 μm-thick layer between two silicon strips. The specimen was cured at 100 °C for 2 h and then allowed to cool slowly to room temperature. The thickness of the specimen was measured by a micrometer after the curing process and the thickness of the epoxy layer was obtained by subtracting the thickness of two silicon adherends from the specimen thickness.

Fracture experiments were conducted at 5 different separation rates, ranging from 0.042 to 8.5 mm/s. For each separation rate, at least 3 specimens were tested to provide a measure of the reliability of the data. We note that, while the applied separation rate was controlled at the opening end of the specimen, the local separation rate at the crack tip depends on the initial crack length as well as the interfacial properties, which cannot be directly controlled in the experiments.

3. Analysis

In this section, we present a series of analyses of the DCB experiments. First, we adopt a beam on elastic foundation (BEF) model that can be used to directly, but approximately, interpret the experimental data. Then, we describe the iterative method that was used to extract the traction-separation relation for cohesive zone modeling of the silicon/epoxy interface at each separation rate. Finally, we propose a rate-dependent cohesive zone model based on the thermally activated bond breaking kinetics and numerically solve the DCB problem at different separation rates.

3.1. Beam on elastic foundation analysis

In the experiment, both the specimen structure and loading conditions were designed to be symmetric for the purpose of maintaining a nominally mode I fracture at the interface (see Mode-mix analysis in Supplementary Material). Therefore, the shear stress at the interface of the DCB specimen was negligible, leaving the normal stress as the primary traction between the silicon and epoxy. Considering only the normal traction, a beam on elastic foundation model as presented in previous studies (Gowrishankar et al., 2012; Wu et al., 2016) was adopted to determine the crack growth and the J-integral based on the measurements of the applied load and displacement (Fig. 2). The beam on elastic foundation model predicts the load-displacement response at the loading point as:

$$P = \frac{3\bar{E}_1 I_1 \Delta}{2a^3}\left(1 + \frac{3}{\lambda a} + \frac{3}{(\lambda a)^2} + \frac{3}{2(\lambda a)^3}\right)^{-1}, \tag{3.1}$$

where P and Δ are the applied force and the opening displacement at the loading point, a is the crack length (measured from the loading point to the crack tip; see Fig. 1a), $I_1 = b_1 {h_1}^3/12$ for the silicon beam with width b_1 and thickness h_1, $\bar{E}_1 = \frac{E_1}{1-\nu_1^2}$, and $\lambda = (\frac{6K_0}{\bar{E}_1 {h_1}^3})^{1/4}$ with K_0 being the stiffness of the elastic foundation.

For the sandwich beam specimen with an epoxy layer, the stiffness K_0 was approximately taken as $K_0 = \bar{E}_2/h_2$ in the previous study (Wu et al., 2016). In this work, a different approach was used to determine the stiffness. By measuring the distance from the epoxy terminus (when the Au/Pd coating was not necessary) to the loading point on the specimen after the silicon was peeled off, the initial crack length a_0 was determined. Then, with the crack length a_0, the initial linear portion of the load-displacement response can be used to determine the stiffness by Eq. (3.1) (shown as the red solid line in Fig. 2a). The value of the stiffness was found to be $K_0 = 7.5 \times 10^{12}\text{N/m}^3$, which is about two orders of magnitude smaller than the value used in the previous study (Wu et al., 2016).

Based on Eq. (3.1), the crack length (beyond the initial length) can be determined from the measurements of P and Δ as

$$a(P, \Delta) = \frac{1}{\lambda}\left[\left(\frac{3\lambda^3 \bar{E}_1 I_1 \Delta}{2P} - \frac{1}{2}\right)^{1/3} - 1\right]. \tag{3.2}$$

The corresponding J-integral for the DCB specimen is (Gowrishankar et al., 2012)

$$J(P, \Delta) = \frac{12P^2}{\lambda^2 \bar{E}_1 {b_1}^2 {h_1}^3}\left[\frac{3\lambda^3 \bar{E}_1 I_1 \Delta}{2P} - \frac{1}{2}\right]^{2/3}. \tag{3.3}$$

As shown in Fig. 2, based on the measured load-displacement response (Fig. 2a) for a DCB specimen, the crack length (Fig. 2b) and the J-integral (Fig. 2c) were calculated by Eq. (3.2) and Eq. (3.3), respectively. The fracture resistance curve (Fig. 2d) was then obtained for each specimen, where the crack extension is defined as $\Delta a = a - a_0$. In all cases, the crack did not grow until the J-integral reached a critical value ($J = \Gamma_0$) corresponding to a critical separation (Δ_0), beyond which the crack grew as the J-integral continued increasing. Eventually, a steady state was reached with a constant J-integral ($J = \Gamma_{ss}$), commonly taken as the fracture toughness of the interface. Moreover, the strength of the interface can be defined as

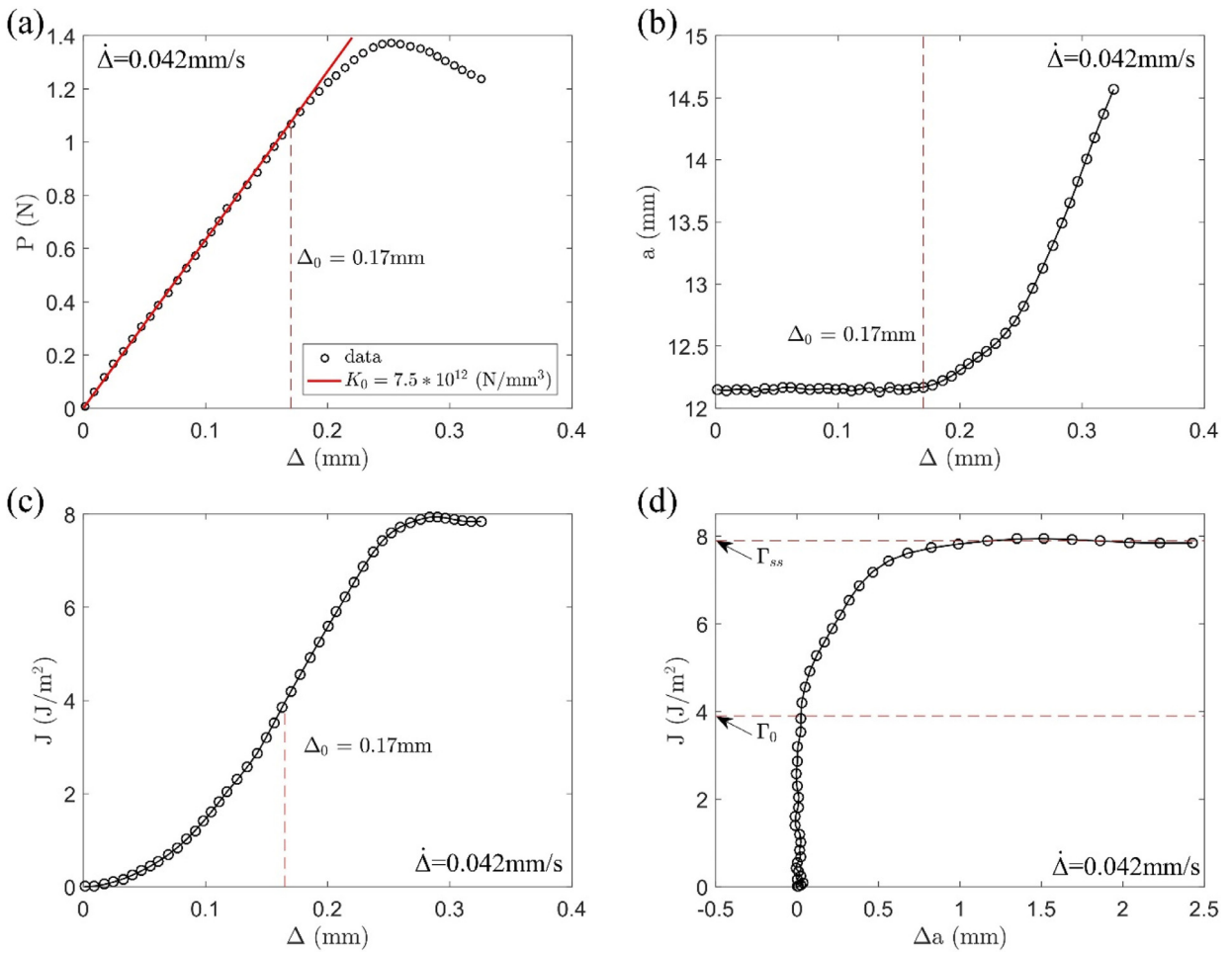

Fig. 2. (a) Measured load-displacement response for a DCB specimen, with the initial linear portion fitted by Eq. (3.1) using the measured initial crack length and the stiffness of the elastic foundation. (b) Crack length determined by Eq. (3.2) versus the applied displacement; (c) J-integral by Eq. (3.3) versus the applied displacement; (d) The fracture resistance curve.

the critical traction for the initiation of crack growth, which may be estimated as $\sigma_0 = \sqrt{2K_0\Gamma_0}$ (assuming a linear traction-separation relation up to the critical traction). As discussed in Section 4, it was found that the fracture resistance curve, the steady-state toughness and the strength are all rate dependent.

3.2. Bilinear traction-separation relations by iterative method

Next, we assume a bilinear traction-separation relation (Fig. 3) for each specimen and determine the parameters by an iterative method. To fully determine a bilinear traction-separation relation, three parameters are required: the elastic stiffness K_0, the interfacial strength σ_0, and the fracture toughness Γ_{ss}. A damage parameter D is used to describe the state of the interface as it evolves from 0 to 1 depending on the local separation:

$$D = \frac{\delta_c(\delta_m - \delta_0)}{\delta_m(\delta_c - \delta_0)}. \tag{3.4}$$

Here, $\delta_0 = \sigma_0/K_0$ is the critical separation for damage initiation, $\delta_c = 2\Gamma_{ss}/\sigma_0$ is the critical separation for fracture, and δ_m is the maximum separation experienced by the interface element. The bilinear traction-separation relation is then given by

$$\sigma = (1 - D)K_0\delta. \tag{3.5}$$

The bilinear traction-separation relation was adopted for the silicon/epoxy interface in a 2D finite element model using the surface interaction module in ABAQUS, similar to previous studies (Gowrishankar et al., 2012; Wu et al., 2016); both silicon strips and the epoxy layer were modeled by four-node plane strain elements (CPE4). For the applied strain rates in this study, the epoxy is assumed to be in its glassy state and hence linearly elastic, and plastic yielding of the epoxy is negligible because the strength of the interface in the present study is well below the yield strength of the epoxy (~75 MPa).

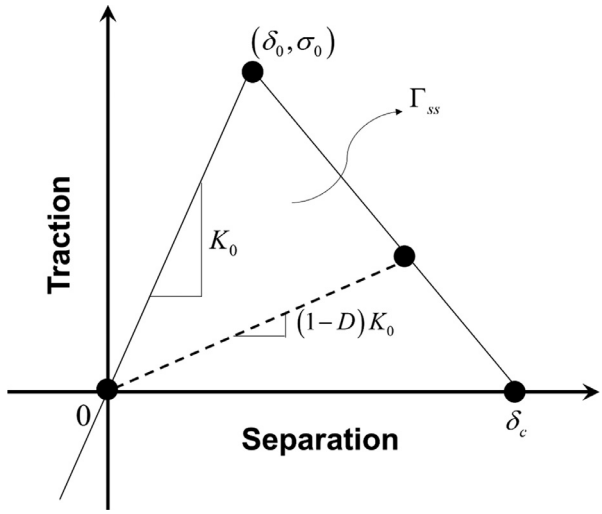

Fig. 3. Schematic of a bilinear traction-separation relation.

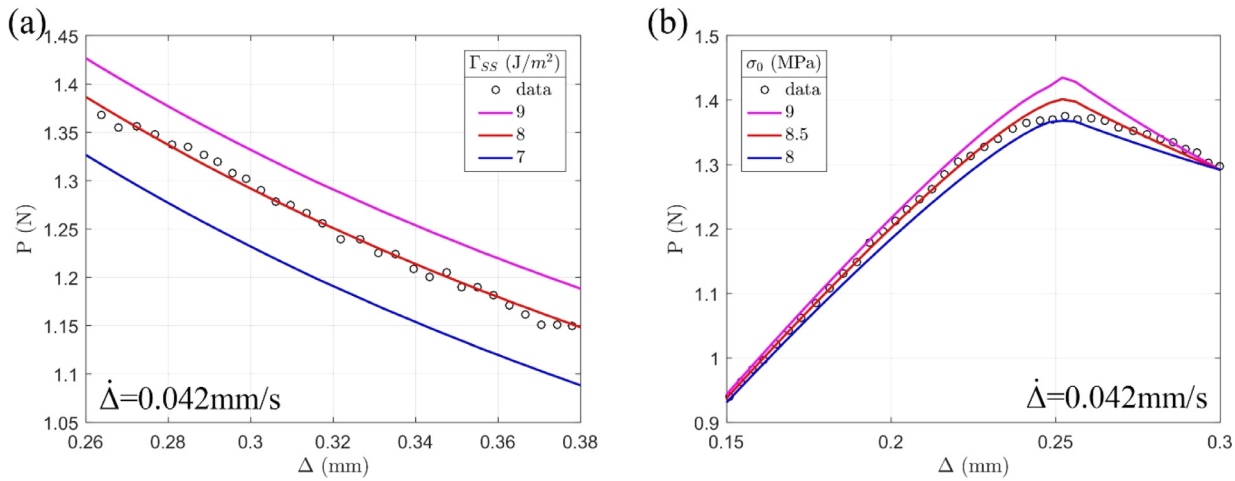

Fig. 4. Comparisons between load-displacement curves from finite element solutions and experimental data. (a) The descending portion varies with the fracture toughness; (b) The response near the peak force varies with the strength of the interface.

For each DCB specimen, we first estimate the three parameters for the bilinear traction-separation relation based on the BEF analysis as discussed in Section 3.1. To improve the accuracy, an iterative approach was adopted to determine the traction-separation relation of the silicon/epoxy interface at each separation rate by comparing the results of the finite element simulation with the measurements. In particular, the initial stiffness K_0 was fully determined by the linear portion of the load-displacement curve (Fig. 2a), which was nearly independent of the separation rate. The other two parameters (Γ_{ss} and σ_0) were determined iteratively following the process outlined by Gowrishankar et al. (2012).

As an example, consider the steps that were taken to identify the parameters for the traction-separation relation at a separation rate of 0.042 mm/s (Fig. 4). The descending portion (Fig. 4a) of the load-displacement curve from the numerical simulations depends sensitively on the value of the fracture toughness. As the first step, ${\sigma_0}^{(0)}$ was fixed at 7.7 MPa and ${\Gamma_{ss}}^{(1)}$ was established as 8 J/m^2. Fig. 4b shows the effect of the interfacial strength on the load-displacement curve near the peak force with the fracture toughness now fixed at ${\Gamma_{ss}}^{(1)} = 8$ J/m^2, where ${\sigma_0}^{(1)} = 8.5$MPa was selected as the strength value. In this case, convergence was achieved (error less than 1%) with only one iteration and thus the two parameters ($\sigma_0 = 8.5$ MPa and $\Gamma_{ss} = 8$ J/m^2) along with $K_0 = 7.5 \times 10^{12}$ N/m^3 give a satisfactory traction-separation relation for this specimen. The same procedure was followed for all specimens in the present study and the results are presented in Section 4.

3.3. A kinetic bond rupture model

The bilinear traction-separation relations determined by the iterative method indicate the rate dependent fracture of the silicon/epoxy interface, which are specific to the applied separation rates in the DCB experiments. To understand possible

origins of the rate dependence and to predict fracture at different rates, a mechanism-based model is needed. In this subsection, we propose a rate-dependent cohesive zone model based on the kinetic bond rupture mechanism as a bottom-up approach, following the spirit of Bell (1978) and Freund (2014).

The fracture of an interface is considered to be the result of thermally activated bond breaking processes. Let $N(t)$ be the number of intact bonds per unit area of the interface at the time t. The rate of thermally activated bond breaking follows the Arrhenius law, namely

$$\frac{\dot{N}(t)}{N(t)} = -\frac{1}{t_0}\exp\left(-\frac{\varepsilon_b}{k_B T}\right), \tag{3.6}$$

where ε_b is the energy barrier that depends on the specific bonds and the force applied to the bonds, and t_0 is a microscopic time scale that depends on temperature T and can be taken as $t_0 = \hbar/(k_B T)$(Hänggi et al., 1990), with Boltzmann constant $k_B = 1.38 \times 10^{-23}$J/K and Planck constant $\hbar = 6.626 \times 10^{-34}$J•s. Eq. (3.6) is essentially the same as Bell's model for cell adhesion but without the bond formation term on the right hand side. Moreover, Eq. (3.6) follows the classical transition-state theory, which turns out to be a special case and upper bound for the more general reaction-rate theory (Hänggi et al., 1990).

As noted by Freund (2014), the statistics of bond breaking for a large number of nominally identical bonds can be reinterpreted equivalently as the survival probability of each single bond. Define the bond survival probability as

$$R(t) = \frac{N(t)}{N_0}, \tag{3.7}$$

where N_0 is the initial number of intact bonds (per unit area). Combining Eqs. (3.6) and (3.7), the bond survival probability follows a rate equation as

$$\frac{\dot{R}}{R} = -\frac{1}{t_0}\exp\left(-\frac{\varepsilon_b}{k_B T}\right). \tag{3.8}$$

A damage parameter D can be defined as the proportion of the broken bonds, which is related to the bond survival probability as:

$$D = 1 - R. \tag{3.9}$$

Then, the evolution of the damage parameter follows a similar rate equation through:

$$\frac{\partial D}{\partial t} = \frac{1-D}{t_0}\exp\left(-\frac{\varepsilon_b}{k_B T}\right). \tag{3.10}$$

The traction transmitted across the interface is proportional to the number of intact bonds per unit area, i.e.$\sigma = N f_b$, with f_b being the force per bond, which can be written as a function of both the separation and the damage parameter, namely,

$$\sigma(\delta, D) = (1-D) f(\delta), \tag{3.11}$$

where $f(\delta)$ is a function that describes the traction-separation relation when there is no bond breaking ($D = 0$). With Eqs. (3.10) and (3.11), we formulate a rate-dependent cohesive zone model, where the energy barrier ε_b and $f(\delta)$ may be determined for specific bonds or interactions. As a simple example, we assume linear functions for both $f(\delta)$ and ε_b as follows:

$$f(\delta) = K_0 \delta, \tag{3.12}$$

$$\varepsilon_b = \varepsilon_0\left(1 - \frac{\sigma}{\sigma_c(1-D)}\right). \tag{3.13}$$

With Eq. (3.12), Eq. (3.11) becomes the same as Eq. (3.5) with an initial stiffness K_0 (which can be related to the individual bond stiffness S_b as $K_0 = N_0 S_b$), but the damage evolution in Eq. (3.10) is rate dependent and different from Eq. (3.4). By Eq. (3.13), the energy barrier for bond breaking is assumed to decrease linearly with the force acting on each bond ($f_b = \sigma/N$)), similar to Bell's model (Bell, 1978), where ε_0 is the equilibrium bond energy and σ_c is a critical stress for instantaneous bond breaking ($\sigma_c = N_0 f_{bc}$), with f_{bc} being the critical force for each bond). When the traction is tensile ($\sigma > 0$), the interfacial bonds are stretched, and the energy barrier is reduced, thus increasing the probability of bond breaking.

A length scale can be defined as: $l_0 = \sigma_c/K_0$, which is the critical separation for instantaneous bond breaking when $D = 0$. Normalizing the traction by σ_c, the separation by the length scale l_0, the time by the time scale t_0, we obtain

$$\bar{\sigma}\left(\bar{\delta}, D\right) = (1-D)\bar{\delta}, \tag{3.14}$$

$$\frac{\partial D}{\partial \bar{t}} = (1-D)\exp\left(-\frac{\varepsilon_0}{k_B T}\left(1-\bar{\delta}\right)\right). \tag{3.15}$$

Now consider the case with a constant separation rate $\dot{\delta}$. By Eqs. (3.14) and (3.15), the normalized traction-separation relation depends on two parameters, the normalized separation rate $\dot{\bar{\delta}} = \dot{\delta} t_0/l_0$ and bond energy $\bar{\varepsilon}_0 = \varepsilon_0/(k_B T)$. For a given

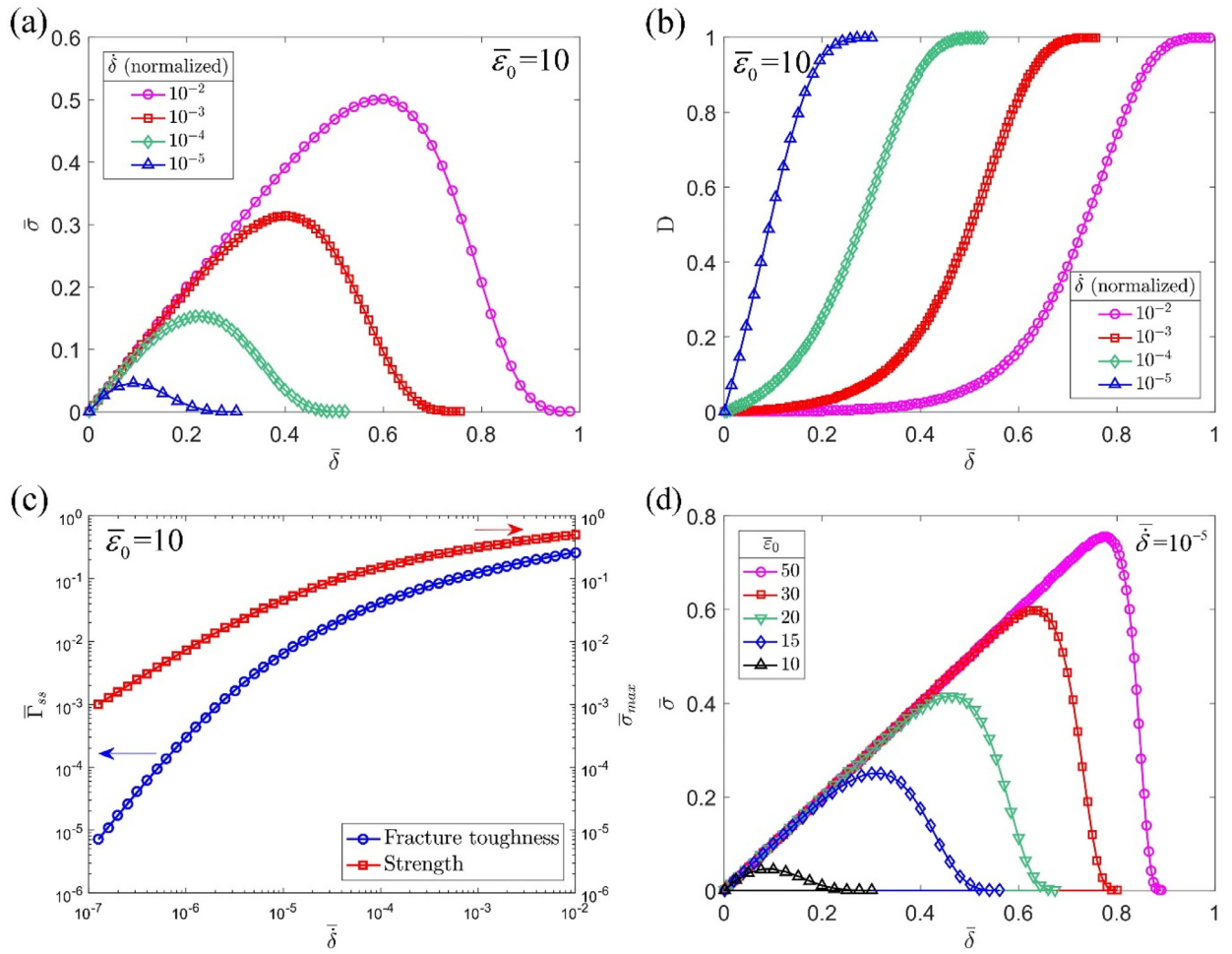

Fig. 5. (a) Normalized traction-separation relations and (b) damage evolution, for different local separation rates; (c) Rate-dependent fracture toughness and strength predicted by the kinetic model; (d) Effect of the normalized bond energy on the traction-separation relation.

bond energy ($\bar{\varepsilon}_0 = 10$), the traction-separation relations (Fig. 5a) and damage evolution processes (Fig. 5b) are both rate dependent. The initial stiffness (K_0) is rate independent, corresponding to the early stage of separation with $D \approx 0$. As the thermally activated bond rupture takes place at the interface, the damage increases and the tangent stiffness decreases. Consequently, the traction first increases and then decreases after a peak value (strength), eventually approaching zero when all bonds are broken ($D = 1$ and $\sigma = 0$). Integrating the traction-separation relation yields the fracture toughness, namely

$$\Gamma_{ss} = \int_0^\infty \sigma \, d\delta. \tag{3.16}$$

Evidently, both the strength (peak traction) and the toughness increase with increasing separation rate (Fig. 5c), qualitatively in agreement with the DCB experiments. By dimensional considerations, the normalized interfacial strength and toughness can be written as

$$\frac{\sigma_{\max}}{\sigma_c} = \bar{\sigma}_{\max}\left(\dot{\bar{\delta}}, \bar{\varepsilon}_0\right), \tag{3.17}$$

$$\frac{\Gamma}{\sigma_c l_0} = \bar{\Gamma}\left(\dot{\bar{\delta}}, \bar{\varepsilon}_0\right). \tag{3.18}$$

The effect of the normalized bond energy is presented in Fig. 5d. As the ratio between the bond energy and the thermal energy ($k_B T$) increases, the softening part of the traction-separation relation becomes more abrupt. In the limiting case when $\bar{\varepsilon}_0 \to \infty$ (e.g., $T = 0$K), the thermally activated bond rupture mechanism would be completely suppressed so that there is no damage evolution, and the traction would increase linearly up to the critical stress σ_c and then drop to zero as all bonds would break instantaneously. For $\bar{\varepsilon}_0 < \infty$, the bond breaking process is thermally activated before the traction reaches the critical level, leading to lower strength and lower toughness. The range of interaction is also reduced as the traction drops

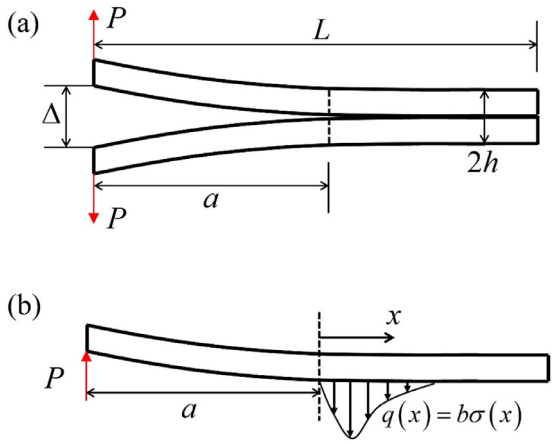

Fig. 6. (a) Schematics of a symmetric DCB specimen; (b) Deflection of one beam with tractions ahead of the crack tip.

to zero before the bonds are stretched to the critical level. This result suggests a temperature effect through the normalized bond energy ($\tilde{\varepsilon}_0 = \varepsilon_0/(k_BT)$). For a given bond energy ε_0, the interfacial strength and toughness decreases with increasing temperature. It should be noted that the temperature also affects the time scale, $t_0 = \hbar/(k_BT)$, which would influence the normalized separation rate.

3.4. A rate-dependent DCB model

In the DCB experiments, the displacements and separation rates were controlled at the loading points, far away from the crack tip. The local separation rate at the crack tip however was different and not controlled. The relation between the global and local separation rates would generally depend on the specific interactions and bond breaking processes, which may be simulated by a cohesive zone model. In a previous study (Gowrishankar et al., 2012), we solved the DCB problem with a *rate-independent*, bilinear traction-separation relation. Here, with the rate-dependent cohesive zone model (Section 3.3), we solve the DCB problem (Fig. 6) to simulate the experiments with different separation rates applied at the loading points, which would allow us to directly compare the model predictions with the experiments.

For a symmetric DCB specimen, the deflection of each beam (Fig. 6b) is related to the interfacial traction by the simple beam equation:

$$\kappa \frac{\partial^4 w}{\partial x^4} = -b\sigma, \tag{3.19}$$

where $\kappa = \tilde{E}_1 I_1$ is the bending modulus of the beam, and by symmetry the interfacial separation is: $\delta = 2w$. The epoxy layer between the two beams is ignored for this analysis. For the interfacial strength and toughness levels that are encountered here, this has been shown to be a reasonable assumption (Wu et al., 2019).

Let $x = 0$ at the initial crack tip ($t = 0$). The DCB specimen is loaded at $x = -a$ with a ramp displacement: $w(x = -a, t) = \dot{\Delta}t/2$, where $\dot{\Delta}$ is the global separation rate. For $-a < x < 0$, the interface is fractured with $D = 1$ (no bonding) and $\sigma = 0$. By Eq. (3.19), the normal crack opening displacement (NCOD) is obtained as (Gowrishankar et al., 2012)

$$\delta(x,t) = \delta^*(t) - x\theta^*(t) + \frac{P(t)a^3}{3\kappa}\left(3\left(\frac{x}{a}\right)^2 + \left(\frac{x}{a}\right)^3\right), \tag{3.20}$$

where $\delta^*(t)$ is the crack-tip opening displacement (CTOD) and $\theta^*(t)$ is the crack-tip opening angle (CTOA), both depending on the interactions ahead of the crack tip. At $x = -a$, $\delta = \dot{\Delta}t$ and the applied force is:

$$P(t) = \frac{3\kappa}{2a^3}\left[\dot{\Delta}t - \delta^*(t) - a\theta^*(t)\right]. \tag{3.21}$$

For $x \geq 0$, the simple beam Eq. (3.19) is coupled with the rate-dependent traction-separation relation given by Eqs. (3.14) and (3.15) in the normalized form. The boundary conditions are: (1) At the crack tip ($x = 0$), the continuity conditions are applied for deflection ($\delta = \delta^*$), rotation ($\delta' = -\theta^*$), bending moment ($\delta'' = 2Pa/\kappa$) and shear force ($\delta''' = 2P/\kappa$); and (2) at the end of the beam ($x = L - a$), the clamped conditions are assumed by setting $\delta = 0$ and $\delta' = 0$. The boundary value problem was then solved numerically by a finite difference method (see Appendix).

When there is no damage evolution ($D = 0$), the DCB problem reduces to the beam on elastic foundation model, with Eq. (3.2) for the load-displacement response. A characteristic length scale for the BEF model is: $l_1 = 1/\lambda$, where $\lambda = (\frac{K_0 b}{2\kappa})^{1/4}$. This length scale is typically much larger than the microscopic length scale for bond breaking ($l_0 = \sigma_c/K_0$). In addition, the

crack length and the beam length are often larger than l_1. To bridge the length scales, we normalize x and the crack length by l_1, but normalize the beam deflection and separation by l_0. Consequently, the beam Eq. (3.19) becomes

$$\frac{\partial^4 \bar{\delta}}{\partial \bar{x}^4} = -4\bar{\sigma}. \tag{3.22}$$

Similarly, in addition to the microscopic time scale (t_0) for the thermally activated bond rupture, the applied global separation rate defines an experimental time scale: $t_1 = l_0/\dot{\Delta}$, which is typically much larger than t_0. It is thus desirable to re-normalize the rate Eq. (3.15) using the experimental time scale t_1 as:

$$\frac{\partial D}{\partial \bar{t}} = \frac{t_1}{t_0}(1-D)\exp\left(-\frac{\varepsilon_0}{k_B T}\left(1-\bar{\delta}\right)\right), \tag{3.23}$$

where the ratio t_0/t_1 is essentially the normalized separation rate applied at the loading point. After re-normalization, the DCB problem depends on four dimensionless parameters: t_0/t_1,$\bar{\varepsilon}_0 = \varepsilon_0/(k_B T)$, $\bar{a} = \lambda a$ (normalized initial crack length), and $\bar{L} = \lambda L$ (normalized specimen length).

Solving the normalized equations in (3.22), (3.23) and (3.14) with normalized boundary conditions (see Appendix), we obtain a normalized load-displacement response for a DCB specimen as shown in Fig. 7a. Here, we take $t_1/t_0 = 10^{10}$,$\bar{\varepsilon}_0 = 30$, $\bar{a} = 15$ and $\bar{L} = 50$. For a constant separation rate ($\dot{\Delta}$), the normalized separation at the loading point is identical to the normalized time ($\bar{\Delta} = \dot{\Delta} t/l_0 = t/t_1 = \bar{t}$). The force at the loading point (Fig. 7a) first increases almost linearly and then decreases, like the experiments (Fig. 2a). The crack-tip opening displacement (CTOD) increases with time monotonically (Fig. 7b), but the local separation rate changes. Initially, when the damage is nearly zero, the CTOD increases almost linearly with a constant local separation rate, as expected from the BEF analysis (Gowrishankar et al., 2012):

$$\dot{\delta}^* = \dot{\Delta}\left(\frac{2}{3}(1+\bar{a})^2 + \frac{1}{3(1+\bar{a})}\right)^{-1}. \tag{3.24}$$

With $\bar{a} >> 1$, the local separation rate at the crack tip is much smaller than the applied separation rate ($\dot{\delta}^* << \dot{\Delta}$). The separation rate at the crack tip starts increasing as the damage accumulates. The damage evolution near the initial crack tip is shown in Fig. 7c. The damage at the crack tip reaches 1 at $\bar{t} = 36.7$, beyond which the crack starts to grow. The change of crack length is shown in Fig. 7d. Interestingly, even after the crack starts growing, the force at the loading point keeps increasing until $\bar{t} \sim 50$ (Fig. 7a), at which point the crack has grown by $\Delta\bar{a} \sim 1$ (Fig. 7d).

The normalized traction-separation relations are shown in Fig. 7e at different locations of the interface ahead of the initial crack tip ($\bar{x} = 0 \sim 4$). Interestingly, the traction-separation relation varies with the location up to $\bar{x} = 2$, after which it becomes independent of the location. As noted earlier, the local separation rate at the initial crack tip is not a constant for the DCB specimen, unlike the case in Fig. 5. Moreover, the loading history could be different at different locations ahead of the initial crack tip, resulting in different traction-separation relations. Eventually, the crack growth reaches a steady-state, after which the traction-separation relation follows the same curve (e.g., $\bar{x} = 3, 4$), indicating the same loading history for every point ahead of the crack tip during the steady-state fracture. In this case (Fig. 7), the steady state is reached when the crack tip advanced to $\bar{x} = 2$ (or $\Delta\bar{a} \sim 2$), corresponding to $\bar{t} \sim 60$. The steady state can also be seen from the damage distribution in Fig. 7c, where a damage zone can be identified ahead of the crack tip with $0 < D < 1$ and remains nearly identical in the steady state. More clearly, by shifting the damage distribution curves to the left by the distance of crack growth, we replot in Fig. S1(a) (see Supplementary Fig. S1) the development of the damage zone ahead of the crack tip, where the damage distributions during the steady state collapse onto the same curve. Moreover, we plot the traction distributions ahead of the crack tip in Fig. S1(b), corresponding to the damage distributions before and after the steady state.

The J-integral of a DCB specimen, by its definition, can be calculated with a contour enclosing the interface from the crack tip ($\bar{x} = 0$) to the clamped end ($\bar{x} = \bar{L} - \bar{a}$), which leads to

$$\bar{J} = \int_0^{\bar{L}-\bar{a}} \bar{\sigma} \cdot \frac{\partial \bar{\delta}}{\partial \bar{x}} d\bar{x}, \tag{3.25}$$

where $\bar{J} = J/(\sigma_c l_0)$ is the normalized J-integral. If the traction-separation relation is identical for all points along the interface, the J-integral in Eq. (3.25) can be reduced to an integral of the traction-separation relation at the initial crack tip, namely

$$\bar{J} = \int_0^{\bar{\delta}^*} \bar{\sigma}\, d\bar{\delta}. \tag{3.26}$$

Eq. (3.26) has been widely used to extract traction-separation relations for rate-independent cohesive zone models (Gowrishankar et al., 2012; Wu et al., 2016). However, for the rate-dependent cohesive zone model considered here, the traction-separation relation at the initial crack tip is different from that in the steady state (Fig. 7e). As a result, Eq. (3.26) is generally incorrect, and Eq. (3.25) should be used instead. As shown in Fig. 7f, by Eq. (3.26), the J-integral remains constant after crack growth, which is actually the J-integral for crack initiation ($J = \Gamma_0$). By Eq. (3.25), the J-integral increases and reaches a steady state value, a typical behavior for a fracture resistance curve (R-curve). Apparently, the J-integral for crack initiation corresponds to the traction-separation relation at the initial crack tip, and the J-integral for the steady state corresponds to the steady-state traction separation relation at a location ahead of the initial crack tip (e.g., $\bar{x} = 3, 4$). We note that,

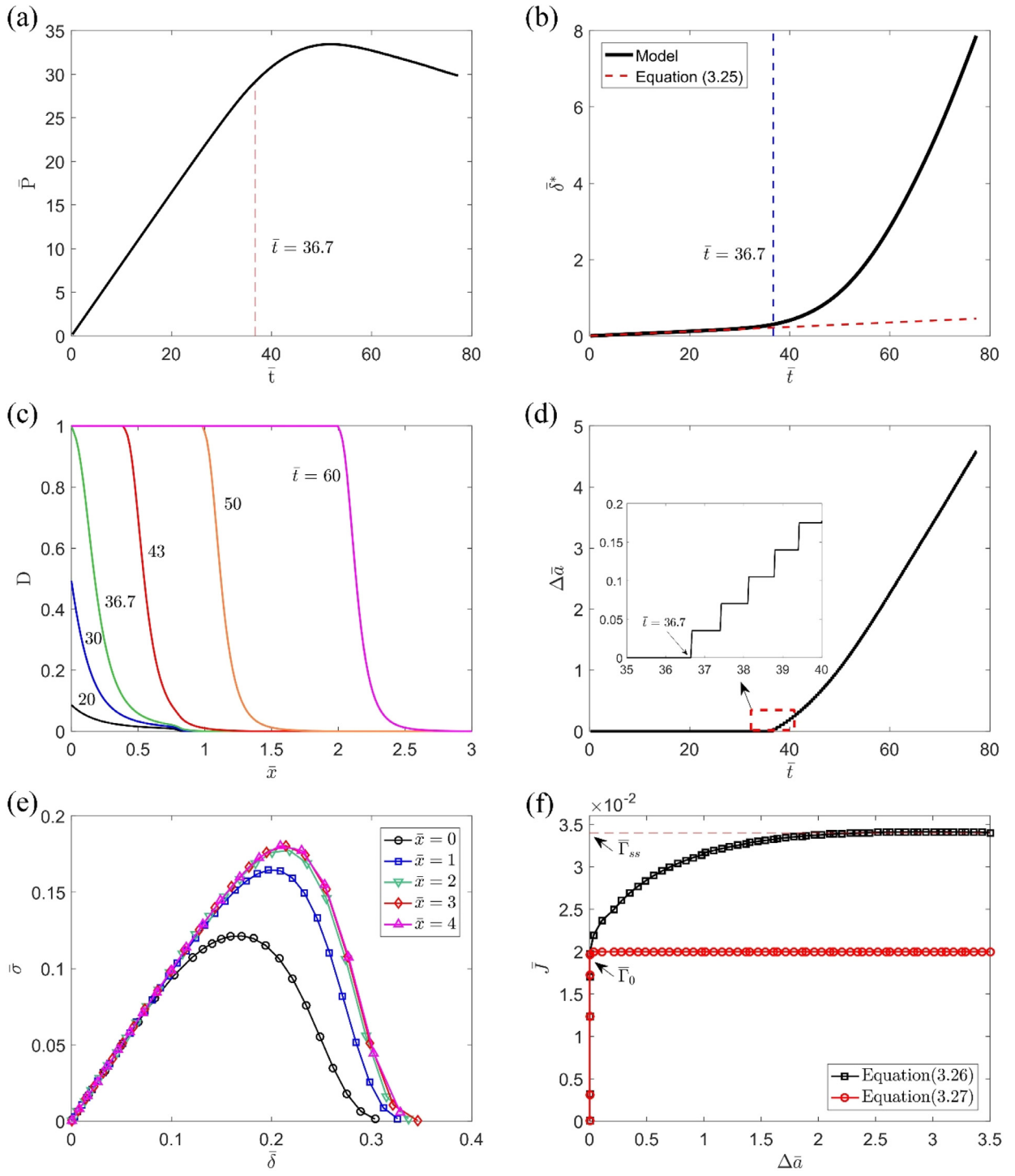

Fig. 7. Numerical results from the rate-dependent DCB model: (a) load-time response; (b) crack-tip opening displacement; (c) damage parameters along the interface at different times; (d) crack growth; (e) traction-separation relations at different locations along the interface; (f) normalized J-integral versus the change of crack length as the fracture resistance curve obtained by Eqs. (3.25) and (3.26).

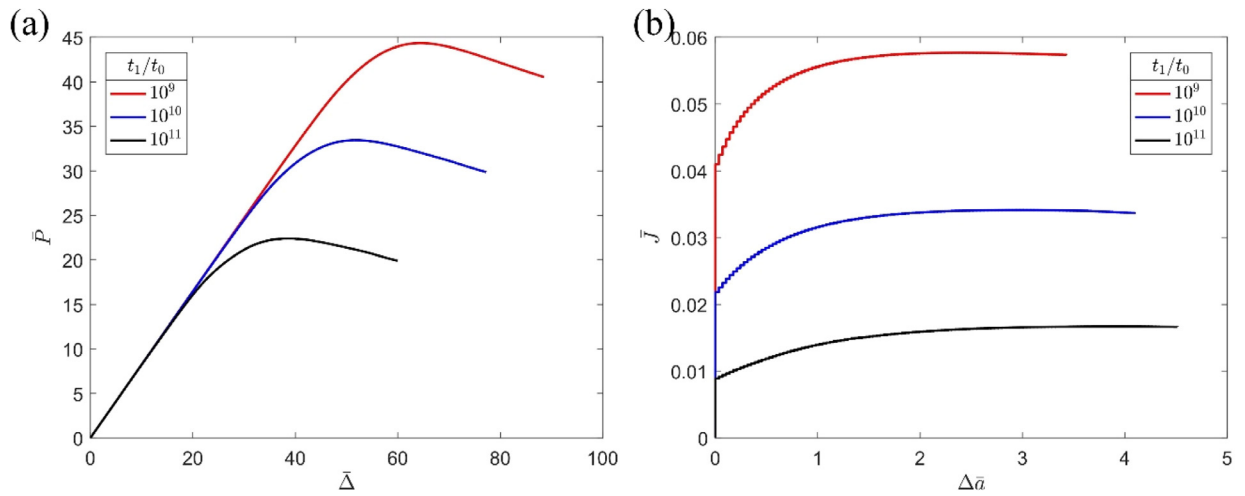

Fig. 8. Predicted rate dependence of the DCB experiment ($\bar{\varepsilon}_0 = 30$, $\bar{a} = 15$ and $\bar{L} = 50$): (a) Normalized load-displacement responses; (b) Normalized fracture resistance curves.

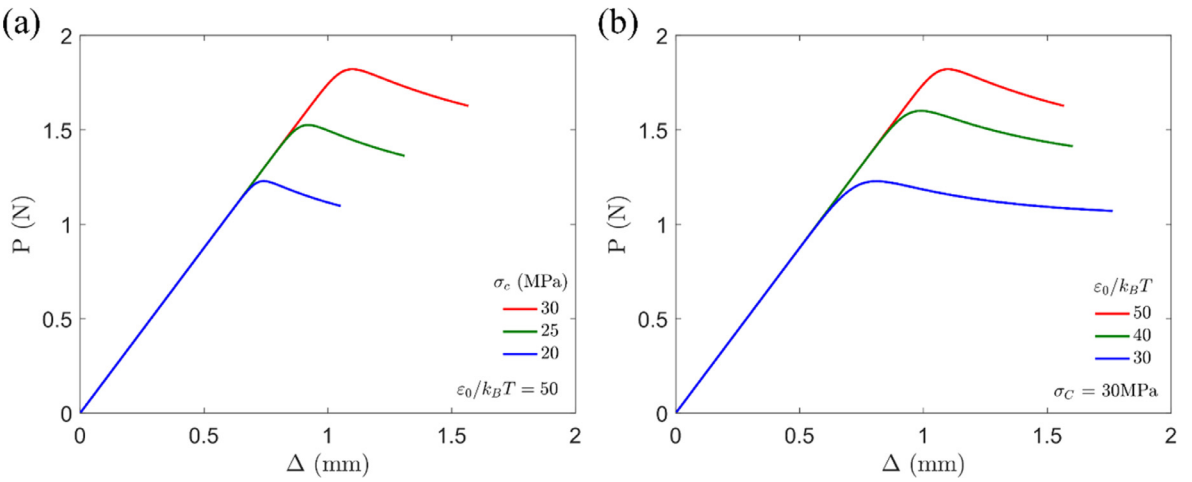

Fig. 9. The effect of (a) the critical stress and (b) the bond energy on the load-displacement responses of DCB specimens ($\dot{\Delta} = 8.5$mm/s, $a_0 = 19$mm, L = 38mm) by the rate-dependent DCB model.

for the rate-independent cohesive zone models, the same traction-separation relation is often assumed for the entire interface, and to predict the R-curve, crack growth is assumed to initiate at the peak traction. For the bilinear traction-separation relation (Fig. 3), the J-integral for crack initiation would be $\Gamma_0 = \sigma_0^2/(2K_0)$ and the steady-state toughness is: $\Gamma_{ss} = \sigma_0\delta_c/2$. Such assumptions are unnecessary for the rate-dependent cohesive zone model, which naturally predicts a rate-dependent R-curve as a result of the kinetic damage evolution process.

The rate-dependent cohesive zone model predicts different load-displacement responses as shown in Fig. 8a for different global separation rates ($t_1/t_0 = 10^{11}, 10^{10}, 10^9$), and the corresponding R-curves are shown in Fig. 8b. With the same parameters for an interface, (t_0,K_0,ε_0,σ_c), as the applied separation rate increases (t_1/t_0 decreasing), the normalized peak force increases and the interface shows more resistance to crack growth, with both the initiation and steady-state J-integrals increasing (Fig. 8b), similar to the R-curves obtained from the DCB experiments (Fig. 10b).

To compare with the DCB experiments, four parameters, (t_0,K_0,ε_0,σ_c), are needed in the rate-dependent cohesive zone model. For all specimens, the microscopic time scale is set by the temperature as $t_0 = \hbar/(k_BT)$ ($\sim 10^{-13}$s), and the stiffness is taken to be $K_0 = 7.5 \times 10^{12}$N/m^3 based on the BEF analysis. The other two parameters, the critical stress (σ_c) and the bond energy (ε_0), both affect the resulting load-displacement response of the DCB experiment. As shown in Fig. 9, the peak force is elevated by an increase in the critical stress or the bond energy, whereas the slope of the descending portion of the load-displacement response decreases as the bond energy decreases. For each specimen, we determine the two parameters by an iterative procedure similar to that in Section 3.2: (i) First, fix the value of the bond energy and select a value for the critical stress so that the model can predict the same peak force as the experimental data; (ii) Next, slightly adjust the

Table 1
Values of the rate-dependent properties of the silicon/epoxy interface associated with the bilinear traction-separation relations obtained from the BEF analysis.

$\dot{\Delta}$ (mm/s)	Specimen No.	h_2 (μm)	a_0 (mm)	K_0 ($\times 10^{12}$ N/m^3)	Γ_0 (J/m^2)	Γ_{ss} (J/m^2)	σ_0 (MPa)
0.042	1	1.2	12.2	7.5	3.9	7.8	7.7
	2	5.1	12.9	6.6	5.3	6.5	8.4
	3	13.3	15.8	7.1	6.8	8.6	9.8
	4	39.3	13.4	7.5	6.1	7.3	9.5
0.42	5	8.0	12.3	8.1	8.0	11.5	11.4
	6	10.2	13.1	6.9	8.1	10.5	10.6
	7	22.0	13.9	7.5	7.1	9.0	10.3
	8	25.7	17.8	6.8	8.0	10.0	11.0
2.1	9	4.5	21.8	7.7	12.5	19.0	13.7
	10	5.1	23.7	6.9	11.0	15.0	12.3
	11	10.2	16.6	6.5	15.5	20.3	14.2
4.2	12	2.5	22.3	8.7	14.0	19.0	15.6
	13	9.0	21.3	8.1	15.4	21.3	15.2
	14	10.8	18.8	6.0	18.7	22.5	15.0
8.5*	15	5.7	17.3	7.5	20.9	22.0	17.7
	16	7.6	19.1		20.0	23.8	17.3
	17	19.1	17.6		20.5	24.5	17.5

* For the case with $\dot{\Delta} = 8.5$ mm/s, the initial crack length was not measured directly. Instead, it was determined by Eq. (3.2) using the average stiffness of the interface, $K_0 = 7.5 \times 10^{12}$ N/m^3, along with the initial slope of the load-displacement response.

value of the bond energy to "rotate" the descending portion of the load-displacement curve; (iii) Repeat steps (i-ii) until the load-displacement response agrees with the experiment satisfactorily. The results are discussed in Section 4.

4. Results and discussion

A total of 17 DCB specimens were used in experiments with at least 3 specimens for each of the 5 applied separation rates (Table 1). The load-displacement response was measured for each specimen (see Supplementary Fig. S2), and Fig. 10a shows five of them, one for each separation rate. In Section 3, we presented three methods to analyze the DCB experiments. First, a direct method based on the beam on elastic foundation (BEF) model can be used to estimate the crack growth and the J-integral. The stiffness of the elastic foundation was determined by fitting the linear portion of the load-displacement curve (Fig. 2a) for each specimen. The results show similar stiffness for different separation rates (Table 1 and Fig. S3a in Supplementary Materials), and the average value, $K_0 = 7.5 \pm 0.5 \times 10^{12}$N/m^3, was then used as the rate-independent stiffness for the subsequent analyses. We note that, by Eq. (3.2), the initial slope of the load-displacement response (Fig. 10a) depends on the initial crack length, which varies from specimen to specimen. In addition, the critical value of the J-integral for initiation of crack growth (Γ_0) and the steady-state fracture toughness (Γ_{SS}) can be estimated directly from the resistance curves (Fig. 10b) following the procedure presented in Section 3.1 (Fig. 2). Then, the strength of the interface can be estimated as $\sigma_0 = \sqrt{2K_0\Gamma_0}$ assuming a bilinear traction-separation relation (Fig. 3). The results for all specimens are summarized in Table 1. Furthermore, we plot the interfacial properties versus the epoxy thickness at each separation rate (see Supplementary Fig. S3). Based on these results, we find: (1) the stiffness (K_0) is independent of the rate or the epoxy thickness (Fig. S3a), and thus can be treated as a constant; (2) the steady-state toughness (Γ_{ss}) and the interfacial strength (σ_0) are independent of epoxy thickness (Fig. S3 b-c) but depend on the seperation rate (Fig. 10c and d); (3) there is no clear dependence of the difference between Γ_0 and Γ_{ss} on the epoxy thickness (Fig. S3d). Overall, the epoxy thickness has a negligible effect on the interfacial properties obtained by the direct method. For all the specimens, the obtained values for the interfacial strength are well below the expected yield strength of the epoxy of ~75 MPa (Na et al., 2015). Therefore, we do not expect any significant plastic deformation in the epoxy. On the other hand, if the strength of the interface were higher than the strength of epoxy, similar to the cases considered by Tvergaard and Hutchinson (1996), large-scale yielding of the epoxy would be expected and the results would then depend on the epoxy thickness. Moreover, since the epoxy is in its glassy state at the room temperature, the effect of bulk viscoelasticity is negligible, and thus the rate dependency is primarily due to the interfacial fracture process.

The values of K_0, σ_0, and Γ_{SS} obtained from the BEF analysis provide the first guess for a bilinear traction-separation relation for each specimen. Then, by the iterative method (Section 3.2), we adjusted the values of σ_0 and Γ_{SS} in the finite element simulations to best fit the load-displacement responses (see Supplementary Fig. S4), although the same stiffness, $K_0 = 7.5 \times 10^{12}$N/m^3, was used in all cases. The traction-separation relations thus obtained are rate dependent as shown in Fig. 10e for the five specimens corresponding to those in Fig. 10a (specimens no. 1, 8, 9, 13, 16 in Table 1). Similar to the BEF results, both the strength and toughness of the silicon/epoxy interface increased as the applied separation rate increased (Fig. 10c and d).

The increase in interfacial toughness and strength with increasing separation rate is interesting because the epoxy being considered here is in its glassy state and the toughness of bulk epoxy specimens decreases with separa-

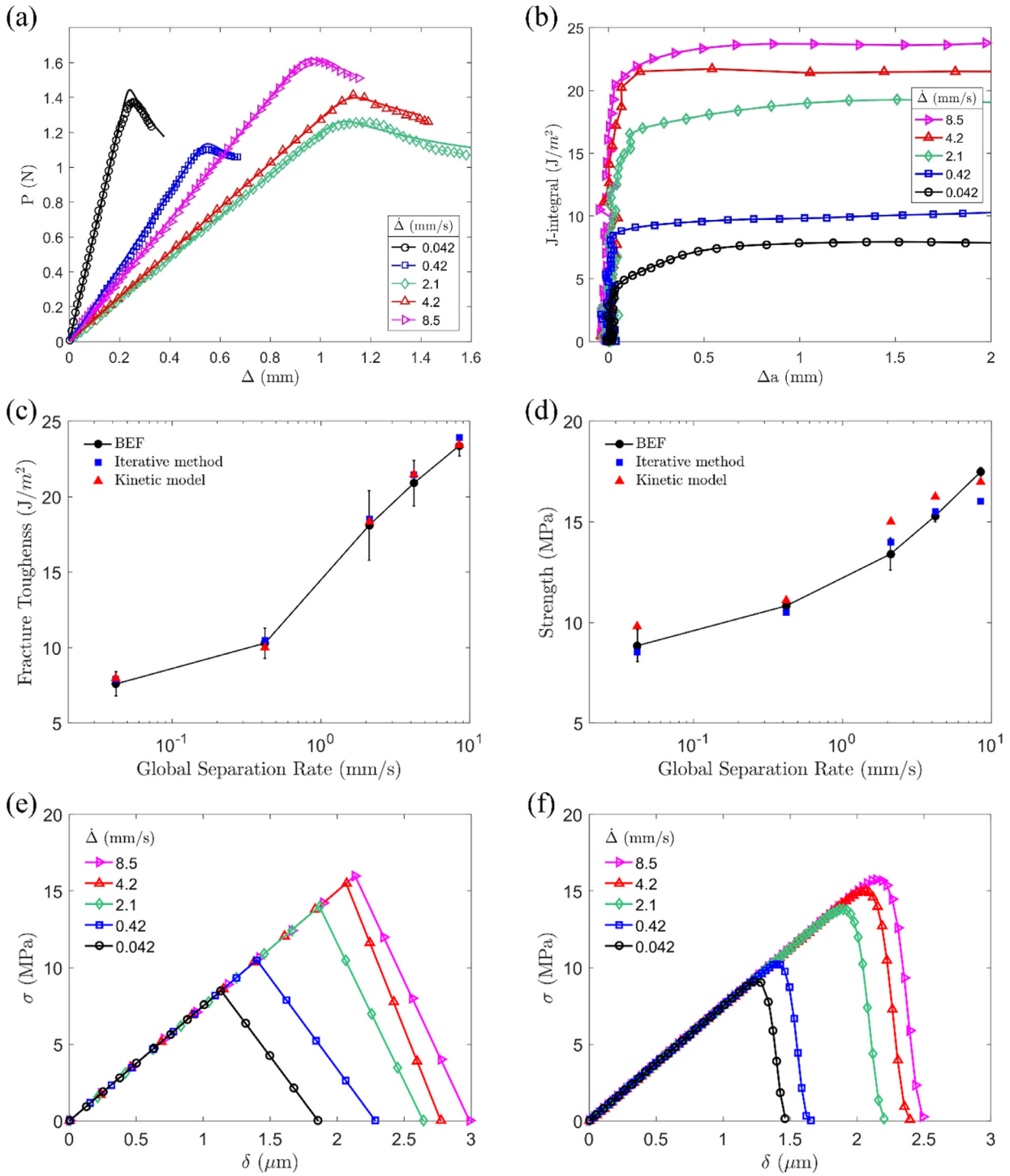

Fig. 10. (a) Load-displacement curves of five specimens with different separation rates, symbols for the measured data and solid lines for the numerical results obtained by the rate-dependent DCB model; (b) Resistance curves for different separation rates by the BEF analysis. Rate dependence of (c) steady-state fracture toughness and (d) interfacial strength obtained by the three methods (the BEF results were averaged over all specimens at each separation rate with error bars showing the standard deviations). (e) Bilinear traction-separation relations obtained by the iterative method; (f) Crack tip traction-separation relations obtained by the rate-dependent DCB model.

Table 2
Values of the parameters for the silicon/epoxy interface associated with the rate-dependent cohesive zone model.

$\dot{\Delta}$ (mm/s)	Specimen No.	a_0 (mm)	$\dot{\delta}^*$ (μm/s)	σ_c (MPa)	Γ_0 (J/m^2)	Γ_{ss} (J/m^2)	σ_0 (MPa)
0.042	1	12.2	0.256	15.7	6.66	7.50	9.68
	2	12.9	0.230	14.4	6.12	6.88	8.91
	3	15.8	0.264	16.3	6.91	7.78	10.1
	4	13.4	0.244	15.2	6.44	7.26	9.40
0.42	5	15.6	2.52	18.0	9.55	10.7	11.8
	6	13.1	2.24	17.3	9.60	10.3	11.3
	7	13.9	2.00	16.0	8.51	9.48	10.5
	8	17.8	1.25	17.0	8.56	9.92	11.0
2.1	9	21.8	4.24	22.3	15.9	18.3	14.8
	10	12.7	3.61	20.5	14.6	16.8	13.6
	11	16.6	7.14	22.7	16.4	18.9	15.2
4.2	12	17.3	8.11	22.8	17.9	20.6	15.4
	13	21.3	8.86	23.5	18.6	21.3	15.9
	14	18.8	11.3	24.3	19.3	22.1	16.5
8.5	15	17.3	26.7	24.2	20.1	23.0	16.8
	16	19.1	22.1	24.7	20.4	23.3	17.0
	17	17.6	25.9	24.5	20.5	23.3	16.9

tion rate (Makhecha et al., 2009). The results presented here for interfacial fracture parallel those presented in Rakestraw et al. (1995) for steel/epoxy interfaces. Thus, it appears that the noted rate dependence may be related to an interphase region (Drzal, 1986; Khanna et al., 2003; Liechti et al., 2000; Liu et al., 2016; Sharpe, 1972; Williams et al., 1990) or the pullout of epoxy ligaments (Neggers et al., 2015; Swadener et al., 1999). In either of these scenarios, bond rupture must be a feature of interfacial failure.

For the third method, we proposed a rate-dependent cohesive zone model based on the kinetic bond rupture mechanism (Section 3.3) and solved the DCB problem numerically (Section 3.4). Ideally, with four parameters, (t_0,K_0,ε_0,σ_c), this model should be able to explain and predict the rate-dependent fracture of a specific interface (e.g., the silicon/epoxy interface) in all specimens. However, in order to fit the experimental data, one of the four parameters (σ_c) had to be adjusted, whereas the other three are constants. In particular, the stiffness is the same as that obtained by the BEF analysis: $K_0 = 7.5 \times 10^{12}$N/m^3. The microscopic time scale is set by the temperature, $t_0 = \hbar/(k_B T)$ ($\sim 10^{-13}$s). The bond energy ε_0 is found to be around 1.5 eV for all specimens. The values of the critical stress are listed in Table 2. Fig. 10a shows the comparison of the load-displacement responses between the numerical results and the experiments for the five specimens at different separation rates. Similar comparisons for all specimens are shown in Supplementary Material Fig. S2.

The bond energy of 1.5 eV is somewhat lower that the values associated with Si-C and Si-H bonds at 4.35 and 2.98 eV, respectively. The extracted critical stress values ranging from 14 to 25 MPa are also lower than the 75 MPa yield strength of this epoxy (Na et al., 2015). These comparisons suggest that the interfacial bonds are not all covalent bonds and could be a mixture of primary and secondary bonds. In addition, bond breaking models that are targeted at specific bonds, as identified, for example, by X-Ray Photoelectron spectroscopy of fracture surfaces (Swadener et al., 1999) may reconcile some of the differences noted here.

The critical stress of the interface may depend on the local separation rate. As noted in Fig. 7b, by the rate-dependent cohesive zone model, the local separation rate at the initial crack tip ($\dot{\delta}^*$) is nearly a constant up to the initiation of crack growth. According to Eq. (3.24), the local separation rate depends on the initial crack length of the DCB specimen and the applied separation rate ($\dot{\Delta}$). By plotting the critical stress versus the local separation rate for all specimens as shown in Fig. 11, we observe an interesting transition: the critical stress is approximately constant at low and high separation rates, but undergoes a transition from about 15.5 MPa to 24.5 MPa for the intermediate separate rates (from 2 to 10 μm/s). This transition suggests possibly different mechanisms for the critical stress at the low and high separation rates, which could be related to other mechanisms such as chain pull-out (Kogan et al., 1996; Xu et al., 1991). Further studies are needed to elucidate the effects of different mechanisms.

With the rate-dependent cohesive zone model, the traction-separation relations at the initial crack tip are shown in Fig. 10f for the five specimens in comparison with the bilinear traction-separation relations in Fig. 10e. As noted in Fig. 7e, the traction-separation relation at the steady-state is different from that at the initial crack tip. Consequently, both the peak stress and the fracture toughness corresponding to the steady-state traction-separation relations are higher than those at the initial crack tip. Fig. 10c compares the steady-state fracture toughness obtained by all three methods and Fig. 10d compares the peak stress, both plotted versus the separation rate ($\dot{\Delta}$) applied at the opening end of the DCB specimen. More appropriately, the interfacial properties are plotted versus the local separation rate ($\dot{\delta}^*$) in Fig. 12.

The fracture toughness and strength obtained by the three methods are comparable overall. The BEF model allowed direct extraction of the interfacial properties, although the damage process during fracture was not explicitly accounted for. By assuming a bilinear traction-separation relation, the iterative method considers the damage process in a particular way, with which the numerical results by finite element analyses could fit the experimental data very well. However, as a

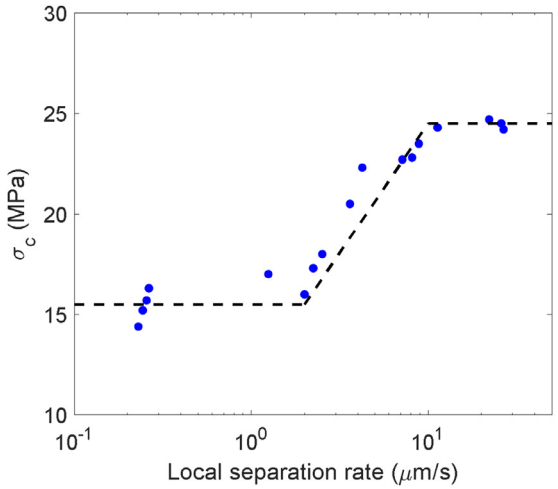

Fig. 11. The critical stress of the interface versus the local separation rate for all specimens.

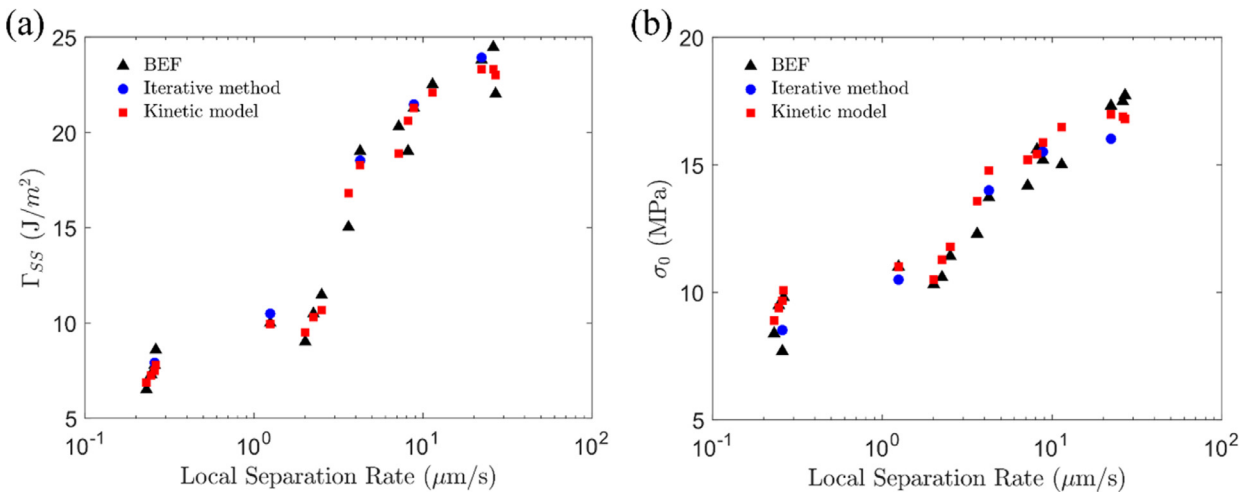

Fig. 12. (a) Steady-state fracture toughness and (b) interfacial strength obtained by the three methods, versus the local separation rates at the crack tip.

phenomenological model, the parameters of the bilinear traction-separation relation must be determined for each specific separation rate and may be limited to specific specimen geometry. Thus, without any specific underlying mechanisms, the phenomenological model would not be predictive of the rate dependence.

By assuming a thermally activated bond rupture mechanism, we have proposed a rate-dependent cohesive zone model, which can be used to explain the rate dependence in the DCB experiments and may be used to predict time and rate-dependent failure of the same interface in other geometries. The comparison with the DCB experiments is promising, although one of the four parameters had to be adjusted for different rates. This caveat may be related to statistical uncertainties with the specimen, where the interfacial bonds may not be identical or intact in all specimens as prepared. It is also possible that other mechanisms not considered in this model may be at play. Nevertheless, the proposed model is intrinsically rate dependent, and the DCB experiments provided clear evidence of similar rate dependency but also revealed the necessity of considering additional mechanisms in order to fully understand the rate-dependent fracture of the specific interface.

5. Conclusions

Silicon/epoxy/silicon sandwich specimens were loaded under nominally mode I conditions over a range of separation rates with a view to examining the rate-dependent fracture of the silicon/epoxy interface. Three methods are used to extract the interfacial properties, including a direct method based on the BEF model, an iterative method with bilinear traction-separation relations, and an intrinsically rate-dependent cohesive zone model. The key findings are summarized as follows.

- The BEF model allowed direct extraction of the interfacial properties, although the damage process during fracture was not explicitly accounted for. The obtained fracture resistance curves are rate dependent for the DCB specimens, with both the steady-state toughness and the strength increasing as the applied separation rate increased.
- By assuming a bilinear traction-separation relation, the iterative method considers the damage process in a particular way, with which the numerical results by finite element analyses could fit the experimental data very well. Similar to the BEF results, both the strength and toughness of the silicon/epoxy interface increased as the applied separation rate increased. However, as a phenomenological model, the parameters of the bilinear traction-separation relation must be determined for each separation rate and may be limited to specific specimen geometry. Without considering any specific mechanisms, such a phenomenological model does not have the capability of predicting the rate dependence.
- A specific mechanism is considered for the intrinsically rate-dependent cohesive zone model. As a fundamental departure from the typical cohesive zone models, the damage evolution is a kinetic process based on thermally activated bond rupture with a microscopic time scale. As a result, the predicted traction-separation relation depends on the local separation rate, with both the toughness and the strength increasing as the local separation rate increased.
- The DCB problem was solved numerically by incorporating the rate-dependent cohesive zone model. Interestingly, the predicted traction-separation relation varies along the interface from the initial crack tip to a particular distance until it reaches a steady state. This is in stark contrast with a typical cohesive zone model that assumes an identical traction-separation relation everywhere along the interface for each specimen. Consequently, rate-dependent fracture resistance curves are predicted by the proposed model, with the J-integral for crack initiation corresponding to the traction-separation relation at the initial crack tip and the steady-state toughness corresponding to the steady-state traction-separation relation at a location ahead of the initial crack tip.
- Ideally, with four parameters, $(t_0,K_0,\varepsilon_0,\sigma_c)$, the proposed rate-dependent cohesive zone model should be able to explain and predict the rate-dependent fracture of a specific interface (e.g., silicon/epoxy interface). However, to fit the experimental data, one of the four parameters (σ_c) had to be adjusted. The critical stress (σ_c) is approximately constant at low and high separation rates, but undergoes a transition from about 15.5 MPa to 24.5 MPa for the intermediate local separate rates (from 2 to 10 μm/s). Further studies are needed to elucidate the underlying mechanisms for this transition.
- Finally, as a perspective, the mechanism-based, rate-dependent cohesive zone model offers a promising step toward modeling rate-dependent fracture of interfaces. In addition, the same model could be used to study time or history dependent fracture such as delayed fracture under static loading and fatigue crack growth under cyclic loading conditions.

Acknowledgments

This work is partially based upon work supported by the National Science Foundation under Cooperative Agreement No. EEC-1160494. Any opinions, findings and conclusions or recommendations expressed in this material are those of the authors and do not necessarily reflect the views of the National Science Foundation.

Supplementary materials

Supplementary material associated with this article can be found, in the online version, at doi:10.1016/j.jmps.2019.06.013.

Appendix A: A finite difference method for the rate-dependent DCB model

By the finite difference method we discretize the normalized beam Eq. (3.22) as

$$\bar{\delta}_{k+2} - 4\bar{\delta}_{k+1} + 6\bar{\delta}_k - 4\bar{\delta}_{k-1} + \bar{\delta}_{k-2} = -4(\Delta\bar{x})^4(1-D_k)\bar{\delta}_k, \tag{A.1}$$

where, $\Delta\bar{x} = \frac{\bar{L}-\bar{a}}{n}$ and $0 \le k \le n$ (with node 0 at the crack tip and node n at the clamped end of the beam). To discretize the boundary conditions, three dummy nodes are used, $(\bar{\delta}_{-2},\bar{\delta}_{-1})$ for the crack tip and $(\bar{\delta}_{n+1})$ for the clamped end. The continuity conditions at the crack tip $(\bar{x}=0)$ are discretized as:

$$\begin{aligned}
&\bar{\delta}_0 = \bar{\delta}^*,\\
&\bar{\delta}_1 - \bar{\delta}_{-1} = -2\Delta\bar{x}\bar{\theta}^*,\\
&\bar{\delta}_1 - 2\bar{\delta}_0 + \bar{\delta}_{-1} = \frac{3(\Delta\bar{x})^2}{\bar{a}^2}\left(2\bar{t} - \bar{\delta}_0 + \bar{a}\frac{\bar{\delta}_1 - \bar{\delta}_{-1}}{2\Delta\bar{x}}\right),\\
&\bar{\delta}_2 - 2\bar{\delta}_1 + 2\bar{\delta}_{-1} - \bar{\delta}_{-2} = \frac{6(\Delta\bar{x})^3}{\bar{a}^3}\left(2\bar{t} - \bar{\delta}_0 + \bar{a}\frac{\bar{\delta}_1 - \bar{\delta}_{-1}}{2\Delta\bar{x}}\right),
\end{aligned} \tag{A.2}$$

and the clamped boundary conditions at $\bar{x} = \bar{L} - \bar{a}$ are:

$$\begin{aligned}
&\bar{\delta}_n = 0,\\
&\bar{\delta}_{n+1} - \bar{\delta}_{n-1} = 0.
\end{aligned} \tag{A.3}$$

The second equation in (A.3) indicates that $\bar{\delta}_{n+1} = \bar{\delta}_{n-1}$, and thus for $k = n-1$ Eq. (A.1) becomes:

$$7\bar{\delta}_{n-1} - 4\bar{\delta}_{n-2} + \bar{\delta}_{n-3} = -4(\Delta\bar{x})^4(1-D_{n-1})\bar{\delta}_{n-1}. \tag{A.4}$$

The corresponding rate equations can be obtained by taking time derivatives of (A.1), (A.2) and (A.4) as:

$$\begin{aligned}
&\dot{\bar{\delta}}_{k+2} - 4\dot{\bar{\delta}}_{k+1} + 6\dot{\bar{\delta}}_k - 4\dot{\bar{\delta}}_{k-1} + \dot{\bar{\delta}}_{k-2} = -4(\Delta\bar{x})^4\left[(1-D_k)\dot{\bar{\delta}}_k - \dot{D}_k\bar{\delta}_k\right],\\
&\left(1-\frac{3\Delta\bar{x}}{2\bar{a}}\right)\dot{\bar{\delta}}_1 - 2\dot{\bar{\delta}}_0\left(1-\frac{3(\Delta\bar{x})^2}{2\bar{a}^2}\right) + \left(1+\frac{3\Delta\bar{x}}{2\bar{a}}\right)\dot{\bar{\delta}}_{-1} = \frac{6(\Delta\bar{x})^2}{\bar{a}^2},\\
&\dot{\bar{\delta}}_2 - 2\dot{\bar{\delta}}_1\left(1+\frac{3(\Delta\bar{x})^2}{2\bar{a}^2}\right) + \frac{6(\Delta\bar{x})^3}{\bar{a}^3}\dot{\bar{\delta}}_0 + 2\dot{\bar{\delta}}_{-1}\left(1+\frac{3(\Delta\bar{x})^2}{2\bar{a}^2}\right) - \dot{\bar{\delta}}_{-2} = \frac{12(\Delta\bar{x})^3}{\bar{a}^3},\\
&7\dot{\bar{\delta}}_{n-1} - 4\dot{\bar{\delta}}_{n-2} + \dot{\bar{\delta}}_{n-3} = -4(\Delta\bar{x})^4\left[(1-D_{n-1})\dot{\bar{\delta}}_{n-1} - \dot{D}_{n-1}\bar{\delta}_{n-1}\right],
\end{aligned} \tag{A.5}$$

which consist of $n+2$ equations ($k = 0, 1, \cdots, n-2$ in the first equation) and can be re-written in a matrix form as:

$$\mathbf{M}\dot{\bar{\boldsymbol{\delta}}} = \mathbf{f} \tag{A.6}$$

where $\dot{\bar{\boldsymbol{\delta}}} = (\dot{\bar{\delta}}_{-2}, \dot{\bar{\delta}}_{-1}, \dot{\bar{\delta}}_0, \ldots\dot{\bar{\delta}}_{n-1})^T$ and

$$\mathbf{M} = \begin{bmatrix}
-1 & 2\left(1+\frac{3(\Delta\bar{x})^2}{2\bar{a}^2}\right) & \frac{6(\Delta\bar{x})^3}{\bar{a}^3} & -2\left(1+\frac{3(\Delta\bar{x})^2}{2\bar{a}^2}\right) & 1 & \ldots & 0 & 0\\
0 & \left(1+\frac{3\Delta\bar{x}}{2\bar{a}}\right) & -2\left(1-\frac{3(\Delta\bar{x})^2}{2\bar{a}^2}\right) & \left(1-\frac{3\Delta\bar{x}}{2\bar{a}}\right) & 0 & \ldots & 0 & 0\\
1 & -4 & 6+4(\Delta\bar{x})^4(1-D_0) & -4 & 1 & \ldots & 0 & 0\\
\vdots & \vdots & \vdots & \vdots & \vdots & \ddots & \vdots & \vdots\\
0 & 0 & 0 & 0 & 0 & \ldots & -4 & 1\\
0 & 0 & 0 & 0 & 0 & \ldots & 6+4(\Delta\bar{x})^4(1-D_{n-2}) & -4\\
0 & 0 & 0 & 0 & 0 & \ldots & -4 & 7+4(\Delta\bar{x})^4(1-D_{n-1})
\end{bmatrix}$$

$$\mathbf{f} = \begin{pmatrix}
\frac{12(\Delta\bar{x})^3}{\bar{a}^3}\\
\frac{6(\Delta\bar{x})^2}{\bar{a}^2}\\
4(\Delta\bar{x})^4\dot{D}_0\bar{\delta}_0\\
\vdots\\
4(\Delta\bar{x})^4\dot{D}_{n-1}\bar{\delta}_{n-1}
\end{pmatrix}. \tag{A.7}$$

By Eq. (3.23), the rate of damage evolution at each node is:

$$\dot{D}_k = \frac{t_1}{t_0}(1-D_k)\exp\left(-\frac{\varepsilon_0}{k_BT}\left(1-\bar{\delta}_k\right)\right). \tag{A.8}$$

Thus, given $\bar{\delta}$ and $\mathbf{D}$ at all nodes, we calculate the damage rate $\dot{\mathbf{D}}$ by (A.8) and then the separation rate $\dot{\bar{\boldsymbol{\delta}}}$ by (A.6). The separation and damage are then updated for the next time step as: ${D_k}^{(i+1)} = {D_k}^{(i)} + \dot{D}_k^{(i)}\cdot\Delta\bar{t}$ and $\bar{\delta}_k^{(i+1)} = \bar{\delta}_k^{(i)} + \dot{\bar{\delta}}_k^{(i)}\cdot\Delta\bar{t}$. For numerical stability and accuracy, the time step was chosen as: $\Delta\bar{t} = 10^{-3}/\max(\dot{D}_k, \dot{\bar{\delta}}_k)$, and a total number of 1001 nodes ($n = 1000$) were used to discretize the beam from $\bar{x} = 0$ to $\bar{x} = \bar{L} - \bar{a}$.

At each time step, the normalized CTOD is $\bar{\delta}^* = \bar{\delta}_0$, and the normalized CTOA is $\bar{\theta}^* = -(\bar{\delta}_1 - \bar{\delta}_{-1})/(2\Delta\bar{x})$. Then, by Eq. (3.21), the normalized force at the loading point ($\bar{x} = -\bar{a}$) is:

$$\bar{P} = \bar{t} - \bar{\delta}^* + \frac{\bar{a}}{2\Delta\bar{x}}\left(\bar{\delta}_1 - \bar{\delta}_{-1}\right), \tag{A.9}$$

where $\bar{P} = \frac{2a^3}{3\kappa l_0}P$.

References

Ackbarow, T., Chen, X., Keten, S., Buehler, M.J., 2007. Hierarchies, multiple energy barriers, and robustness govern the fracture mechanics of alpha-helical and beta-sheet protein domains. Proc. Natl. Acad. Sci. USA 104, 16410–16415.

Barenblatt, G.I., 1962. The mathematical theory of equilibrium cracks in brittle fracture. In: Dryden, H.L., von Kármán, T., Kuerti, G., van den Dungen, F.H., Howarth, L. (Eds.), Advances in Applied Mechanics. Elsevier, pp. 55–129.

Bell, G., 1978. Models for the specific adhesion of cells to cells. Science 200, 618–627.

Büyüköztürk, O., Buehler, M.J., Lau, D., Tuakta, C., 2011. Structural solution using molecular dynamics: fundamentals and a case study of epoxy-silica interface. Int. J. Solids Struct. 48, 2131–2140.

Cheng, H., Wu, J., Yu, Q., Kim-Lee, H.-J., Carlson, A., Turner, K.T., Hwang, K.-C., Huang, Y., Rogers, J.A., 2012. An analytical model for shear-enhanced adhesiveless transfer printing. Mech. Res. Commun. 43, 46–49.

Cox, B.N., Marshall, D.B., 1991. The determination of crack bridging forces. Int. J. Fract. 49, 159–176.

de Gennes, P.G., 1996. Soft adhesives. Langmuir 12, 4497–4500.

Drzal, L.T., 1986. The interphase in epoxy composites. Adv. Polym. Sci. 75 71-32.

Drzal, L.T., 1990. The role of the fiber/matrix interphase on composite interfaces. Vacuum 41, 1615–1618.

Dugdale, D.S., 1960. Yielding of steel sheets containing slits. J. Mech. Phys. Solids. 8, 100–104.

Evans, E., Ritchie, K., 1997. Dynamic strength of molecular adhesion bonds. Biophys. J. 72, 1541–1555.

Feng, X., Meitl, M.A., Bowen, A.M., Huang, Y., Nuzzo, R.G., Rogers, J.A., 2007. Competing fracture in kinetically controlled transfer printing. Langmuir 23, 12555–12560.
Freund, L.B., 2014. Brittle crack growth modeled as the forced separation of chemical bonds within a K-field. J. Mech. Phys. Solids 64, 212–222.
Gao, W., Xiao, P., Henkelman, G., Liechti, M.K., Huang, R., 2014. Interfacial adhesion between graphene and silicon dioxide by density functional theory with van der Waals corrections. J. Phys. D 47, 255301.
Ghatak, A., Vorvolakos, K., She, H., Malotky, D.L., Chaudhury, M.K., 2000. Interfacial rate processes in adhesion and friction. J. Phys. Chem. B 104, 4018–4030.
Giambanco, G., Fileccia Scimemi, G., 2006. Mixed mode failure analysis of bonded joints with rate-dependent interface models. Int. J. Numer. Methods Eng. 67 (, 8), 1160–1192.
Gowrishankar, S., Mei, H., Liechti, K.M., Huang, R., 2012. A comparison of direct and iterative methods for determining traction-separation relations. Int. J. Fract. 177, 109–128.
Hänggi, P., Talkner, P., Borkovec, M., 1990. Reaction-rate theory: fifty years after Kramers. Rev. Mod. Phys. 62, 251.
Hutchinson, J.W., Suo, Z., 1991. Mixed mode cracking in layered materials. Adv. Appl. Mech. 29, 63–191.
Khanna, S.K., Paruchuri, K., Ranganathan, P., Yedla, S.B., Winter, R.M., 2003. Investigation of nanomechanical properties of the interphase in glass fiber reinforced polyester composite using nanoindentation. ASME J. Eng. Mater. Technol. 125, 90–96.
Kinloch, A.J., Williams, J.G., 1980. Crack blunting mechanisms in polymers. J. Mater. Sci. 15, 987–996.
Knauss, W.G., 1975. Fracture mechanics and time dependent strength of adhesive joints. J. Comp. Mat. 5, 39–61.
Knauss, W.G., Losi, G.U., 1993. Crack propagation in a nonlinearly viscoelastic solid with relevance to adhesive bond failure. J. Appl. Mech. 60, 793–801.
Kogan, L., Hui, C.Y., Ruina, A., 1996. Theory of chain pull-out and stability of weak polymer interfaces. 1. Macromolecules 29, 4090–4100.
Landis, C.M., Pardoen, T., Hutchinson, J.W., 2000. Crack velocity dependent toughness in rate dependent materials. Mech. Mater. 32, 663–678.
Lau, D., Büyüköztürk, O., Buehler, M.J., 2012. Characterization of the intrinsic strength between epoxy and silica using a multiscale approach. J. Mater. Res. 27, 1787–1796.
Li, S., Thouless, M.D., Waas, A.M., Schroeder, J.A., Zavattieri, P.D., 2005. Use of mode-I cohesive-zone models to describe the fracture of an adhesively-bonded polymer-matrix composite. Compos. Sci. Technol. 65, 281–293.
Liechti, K., Wu, J.-D., 2001. Mixed-mode, time-dependent rubber/metal debonding. J. Mech. Phys. Solids 49, 1039–1072.
Liechti, K.M., Shirani, A., Dillingham, R.G., Boerio, F.J., Weaver, S.M., 2000. Cohesive zone models of polyimide/aluminum interphases. J. Adhes. 73, 259–297.
Liu, Z., Moore, J.A., Liu, W.K., 2016. An extended micromechanics method for probing interphase properties in polymer nanocomposites. J. Mech. Phys. Solids 95, 663–680.
Makhecha, D.P., Kapania, R.K., Johnson, E.R., Dillard, D.A., Jacob, G.C., Starbuck, J.M., 2009. Rate-dependent cohesive zone modeling of unstable crack growth in an epoxy adhesive. Mech. Adv. Mater. Struct. 16, 12–19.
Marzi, S., Hesebeck, O., Brede, M., Kleiner, F., 2009. A rate-dependent cohesive zone model for adhesively bonded joints loaded in mode I. J. Adhes. Sci. Technol. 23, 881–898.
Mello, A.V., Liechti, K.M., 2006. The effect of self-assembled monolayers on interfacial fracture. J. Appl. Mech. 73, 860–870.
Mohammed, I.K., Charalambides, M.N., Kinloch, A.J., 2016. Modeling the effect of rate and geometry on peeling and tack of pressure-sensitive adhesives. J. Nonnewton Fluid Mech. 233, 85–94.
Na, S.R., Suk, J.W., Tao, L., Akinwande, D., Ruoff, R.S., Huang, R., Liechti, K.M., 2015. Selective mechanical transfer of graphene from seed copper foil using rate effects. ACS Nano 9, 1325–1335.
Neggers, J., Hoefnagels, J.P.M., Van Der Sluis, O., Geers, M.G.D., 2015. Multi-scale experimental analysis of rate dependent metal–elastomer interface mechanics. J. Mech. Phys. Solids 80, 26–36.
Pobelov, I.V., Lauritzen, K.P., Yoshida, K., Jensen, A., Mészáros, G., Jacobsen, K.W., Strange, M., Wandlowski, T., Solomon, G.C., 2017. Dynamic breaking of a single gold bond. Nat. Commun. 8, 15931.
Qian, J., Lin, J., Xu, G.-K., Lin, Y., Gao, H., 2017. Thermally assisted peeling of an elastic strip in adhesion with a substrate via molecular bonds. J. Mech. Phys. Solids 101, 197–208.
Rahul-Kumar, P., Jagota, A., Bennison, S.J., Saigal, S., Muralidhar, S., 1999. Polymer interfacial fracture simulations using cohesive elements. Acta Mater. 47, 4161–4169.
Rakestraw, M., Taylor, M., Dillard, D., Chang, T., 1995. Time dependent crack growth and loading rate effects on interfacial and cohesive fracture of adhesive joints. J. Adhes. 55, 123–149.
Sharpe, L.H., 1972. The interphase in adhesion. J. Adhes. 4, 51–64.
Sørensen, B.F., Jacobsen, T.K., 2003. Determination of cohesive laws by the J integral approach. Eng. Fract. Mech. 70, 1841–1858.
Sorensen, L., Botsis, J., Gmür, T., Humbert, L., 2008. Bridging tractions in mode I delamination: measurements and simulations. Compos. Sci. Technol. 68, 2350–2358.
Spearot, D.E., Jacob, K.I., McDowell, D.L., 2004. Non-local separation constitutive laws for interfaces and their relation to nanoscale simulations. Mech. Mater. 36, 825–847.
Swadener, J.G., Liechti, K.M., de Lozanne, A.L., 1999. The intrinsic toughness and adhesion mechanism of a glass/epoxy interface. J. Mech. Phys. Solids 47, 223–258.
Tvergaard, V., Hutchinson, J.W., 1996. On the toughness of ductile adhesive joints. J. Mech. Phys. Solids 44 (, 5), 789–800.
Wang, P., Gao, W., Huang, R., 2016. Entropic effects of thermal rippling on van der Waals interactions between monolayer graphene and a rigid substrate. J. Appl. Phys. 119, 074305.
Wiita, A.P., Ainavarapu, S.R.K., Huang, H.H., Fernandez, J.M., 2006. Force-dependent chemical kinetics of disulfide bond reduction observed with single–molecule techniques. Proc. Natl. Acad. Sci. 103, 7222–7227.
Williams, J.G., Hodgkinson, J.M., 1981. Crack-blunting mechanisms in impact tests on polymers. Proc. R. Soc. Lond. A 375, 231–247.
Williams, J.G.D., M., E., James, M.R., Morris, W.L., 1990. Properties of the interphase in organic matrix composites. Mater. Sci. Eng. A 126, 305–312.
Wu, C., Gowrishankar, S., Huang, R., Liechti, K.M., 2016. On determining mixed-mode traction–separation relations for interfaces. Int. J. Fract. 202, 1–19.
Wu, C., Huang, R., Liechti, K.M., 2019. Simultaneous extraction of tensile and shear interactions at interfaces. J. Mech. Phys. Solids 125, 225–254.
Xu, C., Siegmund, T., Ramani, K., 2003. Rate-dependent crack growth in adhesives: I. Modeling approach. Int. J. Adhes. Adhes. 23, 9–13.
Xu, D.B., Hui, C.Y., Kramer, E.J., Creton, C., 1991. A micromechanical model of crack growth along polymer interfaces. Mech. Mater. 11, 257–268.
Yoon, T., Shin, W.C., Kim, T.Y., Mun, J.H., Kim, T.-S., Cho, B.J., 2012. Direct measurement of adhesion energy of monolayer graphene as-grown on copper and its application to renewable transfer process. Nano Lett. 12, 1448–1452.
Zhang, X., Mai, Y.-W., Jeffrey, R.G., 2003. A cohesive plastic and damage zone model for dynamic crack growth in rate-dependent materials. Int. J. Solids Struct. 40, 5819–5837.
Zhu, Y., Liechti, K.M., Ravi-Chandar, K., 2009. Direct extraction of rate-dependent traction-separation laws for polyurea/steel interfaces. Int. J. Solids Struct. 46, 31–51.